Modelling of a High-temperature Thermochemical Storage Reactor with Radial Flow across an Annular Packed Bed using the CaCO₃-CaO Cycle as a Model Reaction

Michael Wild[1] and Aldo Steinfeld[1]

[1] Department of Mechanical and Process Engineering, ETH Zürich, 8092 Zurich, Switzerland

Abstract

A heat and mass transfer model of an annular packed-bed reactor utilizing reversible gas-solid reactions is developed for the thermochemical storage of high-temperature solar heat. The governing equations, boundary conditions and numerical implementation are described and the temperature- and state-dependent material properties are presented. The feasibility of this reactor concept is demonstrated through the numerical simulation of a representative scenario utilizing the thermal decomposition of calcium carbonate into calcium oxide and CO_2 as a model reaction. The results of this simulation are presented and discussed.

Keywords: Solar, Thermochemical, Storage, Heat Storage, Carbonation, Calcination.

1. Introduction

Concentrated solar power (CSP) plants use sun-tracking mirror optics to concentrate the direct normal solar irradiation into a solar receiver. The resulting high-temperature heat can then be used to drive heat engines for electricity generation or drive thermochemical processes for fuels and materials production (Romero and Steinfeld, 2012). The operation of CSP plants is constrained by the intermittency of solar radiation, requiring the storage of solar heat to ensure continuous and around-the-clock dispatchability. Three forms of thermal energy storage (TES) are generally considered: sensible, latent and thermochemical (Kuravi et al., 2013). Sensible heat storage utilizes the heat capacity of the storage material; latent heat storage (LHS) utilizes the heat of phase change in the storage material; thermochemical storage (TCS) utilizes the reaction enthalpy of reversible endothermic/exothermic reactions (Agrafiotis et al., 2016; André et al., 2016). TCS can be coupled to a thermocline-based SHS (Agrafiotis et al., 2015; Ströhle et al., 2017), similar to the coupling of LHS and SHS using a packed bed of rocks (Zanganeh et al., 2015, 2014). With such an arrangement, the TCS section acts as a control unit to the SHS section and alleviates the drawbacks of thermocline-based storage, i.e. thermocline degradation and associated heat transfer fluid (HTF) outlet temperature drop during discharging.

The thermochemical reaction considered is the decomposition of a solid, represented by A(s) = B(s) + C(g). Examples are the thermal reduction of metal oxides (Block and Schmü, 2016; Bush and Loutzenhiser, 2018; Muroyama et al., 2015) and the decomposition of carbonates (André et al., 2016; Gigantino et al., 2019; Kyaw et al., 1996), which are characterized by their high gravimetric energy density. In this study, the decomposition of limestone is selected as a model reaction:

$$CaCO_3(s) = CaO(s) + CO_2(g) \qquad \Delta H_{298\ K} = 177.8\ kJ/mol$$
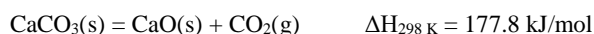
This reaction is thermodynamically favorable at 1158 K and 1 bar. The reaction equilibrium and thus indirectly the reaction rate can be influenced by adjusting the gas pressure and temperature inside the storage reactor (Ströhle et al., 2017).

Nomenclature

Greek Letters

α, β	Stoichiometric Coefficients [-]
Γ	Mass Fraction [-]
ε	Void Fraction [-]
ϵ	Emissivity [-]
γ	Fitting Coefficient [div.]
λ	Themal Conductivity [W·m^{-1}·K^{-1}]
ρ	Density [kg·m^{-3}]
X	Reaction Extent [-]
Ψ_s	Volume-specific Molar Reaction Rate [mol·s^{-1}·m^{-3}]
μ	Dynamic Viscosity [Pa·s]
λ	Thermal Conductivity [W·m^{-1}·K^{-1}]
γ	Empirically Fitted Parameter [div.]
ϕ	Ratio Fluid Film Thickness – Particle Diameter [-]
σ	Ratio Distance Particle Centers – Diameter [-]
ω	Ratio Eff. Length Particle – Diameter [-]

Subscripts

f	Fluid
s	Solid
p	Particle
b	Bed
A,B,C	Species A,B,C
c	Control
ext	External
amb	Ambient
eq	Equilibrium
eff	Effective
rv	Radiation Void-to-Void
rs	Radiation Solid-to-Solid

Superscripts

0	Initial Value

Dimensionless numbers

Bi	Biot number [-]
Nu	Nusselt Number [-]
Pr	Prandtl Number [-]
Re	Reynolds Number [-]

Roman Letters

A	Area [m^2]
V	Volume [m^3]
M	Molar Mass [kg·mol^{-1}]
m	Mass [kg]
n	Molar Amount [mol]
t	Time [s]
$\hat{u}$	Superficial Gas Velocity [m·s^{-1}]
r	Radial Coordinate [m]
p	Pressure [Pa]
K	Permeability [m^2]
e	Sensible Internal Energy [J·m^{-3}]
T	Temperature [K]
k_h	Heat Transfer Coefficient [W·m^{-2}·K^{-1}]
a_v	Volume-specific Surface Area [m^{-1}]
c_p	Heat Capacity [J·kg^{-1}·K^{-1}]
d_p	Particle Diameter [m]
$\bar{R}$	Specific Gas Constant [J·kg^{-1}·K^{-1}]
ΔH_R	Reaction Enthalpy [J·mol^{-1}]
k_0	Rate Constant [s^{-1}]
a,b,c,s	Empirically Fitted Parameters [div.]
E_A	Activation Energy [J·mol^{-1}]
h	Heat Transfer Coefficient [W·m^{-2}·K^{-1}]
Q	Heat [J]
$\dot{q}$	Rate of Heat Flow [W]

Acronyms

CSP	Concentrated Solar Power
TES	Thermal Energy Storage
HTF	Heat Transfer Fluid
SHS	Sensible Heat Storage
LHS	Latent Heat Storage
TCS	Thermochemical Heat Storage

In the present paper, we propose a unique design of a TCS reactor with some intriguing features in terms of simplicity of fabrication and operation, and develop a rigorous numerical heat and mass transfer model of such a reactor for simulating its operation and optimizing its design. Previous models of TCS reactors have been developed for packed-bed tubular reactors with axial flow (Dixon and Nijemeisland, 2001; Ströhle et al., 2014) and annular bed reactors with radial flow (Davis and Watson, 1986; Davis and Yamanis, 1984). The present model is concerned with a tubular reactor with radial flow across a packed bed of small particles ($d_p < 0.2$ mm), and incorporates radiative heat transfer and temperature-dependent material properties because of the high operational temperatures. This reactor concept allows uniform heat release/uptake over the length of the reactor, thereby ensuring controllability.

2. Reactor configuration

Fig. 1 shows the schematic cross-section view of the combined TCS/SHS system where the TCS section is added to the top of the SHS section. The proposed TCS section consists of layered array of parallel reactor tubes in a crossflow configuration to the HTF flowing through the combined TCS/SHS system and delivering/withdrawing heat by convection. Each tubular reactor consists of a gas-tight outer cylindrical shell, a concentric porous gas-feeding inner tube, and a packed bed of powdered/granulated solids filling the annular gap between them. During charging, heat transferred by convection from the HTF to the outer shell is conducted inwards radially across the solid (CaCO$_3$), driving the endothermic decarbonation reaction. The produced gas (CO$_2$) is drawn out through the porous center tube.

During the discharging phase, the reacting gas (CO_2) is pumped back into the reactor in reverse direction, where it recombines with the solid (CaO) driving the exothermic carbonation reaction at higher pressure. Understanding the limiting mechanisms of such a reactor system is key to optimization of the design. The design parameters include: dimensions, number of tubes, gas flow rates, solid morphology (e.g. powder, granules, pellets) and their properties, and operating conditions (e.g. outflow gas temperature).
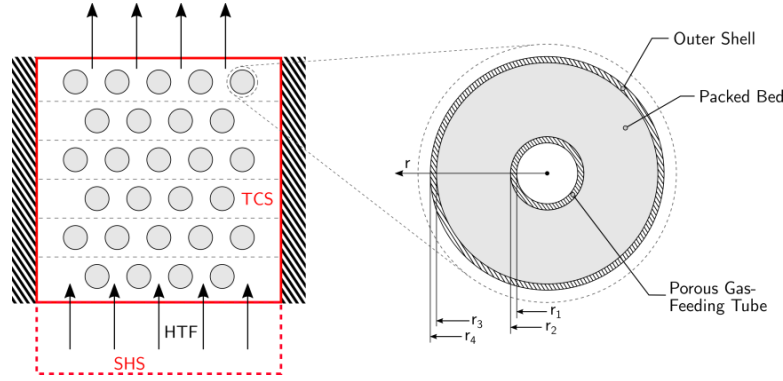

Fig. 1: *Left:* **Schematic configuration (cross section) of the combined sensible-thermochemical thermal energy storage system. The thermochemical storage (TCS) section is located on top of the sensible heat storage (SHS) section and the heat transfer fluid (HTF) is flowing across both sections. The TCS itself consists of stacked layers of parallel tubular reactors.** *Right:* **Cross section of a single tubular reactor: it consists of a gas-tight outer cylindrical shell, a concentric porous gas-feeding inner tube, and a packed bed of powdered/granulated solids filling the annular gap between them.**

3. Reactor Model

3.1 Domain

The modelling domain of a single tubular reactor is shown in Figure 1 (right) and comprises the packed bed filling the annular gap between the outer shell and the gas-feeding porous inner tube. The following simplifying assumptions are made: 1-D infinitely long reactor tube without angular/axial gradients, negligible influence of gravity, uniform shell temperature, uniform temperature within solid particle (justified by Bi << 1 in the pertinent temperature and pressure range), and uniform void fraction in the packed bed. The packed bed is modelled as a two-phase solid/fluid region, where the mass and energy conservation equations are solved for the gas phase, the energy conservation equation is solved for the solid phase, and phases are coupled by heat and mass transfer terms. The heat flux from the HTF serves as a von Neumann boundary condition at the outer shell.

3.2 Chemical reaction

The generic thermal dissociation reaction $\alpha \cdot A(s) \leftrightarrow \beta \cdot B(s) + \gamma \cdot C(g)$ is considered. The reaction extent is defined as:

$$\text{X} = \frac{n_A}{n_A + \frac{\alpha}{\beta} n_B} \tag{1}$$

where n_A and n_B are the molar amounts of species A and B, and α and β their respective stoichiometric coefficients. The volume-specific molar reaction rate is defined:

$$\Psi_s = \frac{\varepsilon_b \rho_s}{M_s} \frac{\partial \text{X}}{\partial t} \tag{2}$$

where the (lumped) reaction kinetic rate is modelled as

$$\frac{\partial X}{\partial t} = k_0 \exp\left(\frac{-E_A}{RT_s}\right) X^a (1-X)^b \left|1 - \frac{p_c}{p_{eq}}\right|^s \tag{3}$$

where k_0 is the rate constant, E_A the activation energy, and p_{eq} the equilibrium partial pressure of the reaction which is found using a fit to tabulated data:

$$p_{eq} = c_0 \cdot c_1 {}^\wedge \left(c_2 + \frac{c_3}{T}\right) \tag{4}$$

3.3 Governing Equations

Let V_p be the volume of the solid particles,

$$V_p = (1 - \varepsilon_b)V \tag{5}$$

where V is the total reactor volume and ε_b is the bed void fraction. The volume of the solid reactant is $V_{p,s} = (1 - \varepsilon_p)V_p$, where ε_p is the particle void fraction. The initial (known) mass fractions of reactants are defined as

$$\Gamma_A^0 = \frac{m_A^0}{m^0} \text{ and } \Gamma_B^0 = \frac{m_B^0}{m^0} \tag{6}$$

The measured initial bed density is defined as $\rho_b^0 = \frac{m^0}{V}$. Thus, the initial amounts of moles present in the reactor are

$$n_A^0 = \frac{V\rho_b^0 \Gamma_A^0}{M_A} \text{ and } n_B^0 = \frac{V\rho_b^0 \Gamma_B^0}{M_B} \tag{7}$$

Using eqn. (1), the amounts of moles of species A and B are found in relation to X:

$$n_A = X\left(n_A^0 + \frac{\alpha}{\beta}n_B^0\right) \text{ and } n_B = (1-X)\left(\frac{\beta}{\alpha}n_A^0 + n_B^0\right) \tag{8}$$

which, using eqn. (7), leads to the masses of the respective species in relation to X:

$$m_A = XV\rho_b^0 \left(\Gamma_A^0 + \frac{\alpha}{\beta}\frac{M_A}{M_B}\Gamma_B^0\right) \text{ and } m_B = (1-X)V\rho_b^0 (\frac{\beta}{\alpha}\frac{M_B}{M_A}\Gamma_A^0 + \Gamma_B^0) \tag{9}$$

The apparent solid density inside the particle is then

$$\rho_S(X) = \frac{m_A + m_B}{(1-\varepsilon_b)V} = \frac{\rho_b^0}{(1-\varepsilon_b)}\left[X\left(\Gamma_A^0 + \frac{\alpha}{\beta}\frac{M_A}{M_B}\Gamma_B^0\right) + (1-X)\left(\frac{\beta}{\alpha}\frac{M_B}{M_A}\Gamma_A^0 + \Gamma_B^0\right)\right] \tag{10}$$

Fluid Phase – The fluid mass conservation equation is given by:

$$\varepsilon_b \frac{\partial \rho_f}{\partial t} + \nabla \cdot (\rho_f \hat{u}) = M\Psi_s \tag{11}$$

where ε_b is the bed porosity, ρ_f is the fluid density, $\hat{u}$ is the superficial gas velocity, M is the molar mass of the gaseous reactant and Ψ_s is the volume-specific molar reaction rate. Written in 1-D cylindrical coordinates and assuming radial symmetry,

$$\varepsilon_b \frac{\partial \rho_f}{\partial t} + \frac{1}{r}\frac{\partial}{\partial r}(r\rho_f \hat{u}) = M\Psi_s \tag{12}$$

The Darcy law for porous media is given by:

$$\nabla p = -\frac{\mu}{K}\hat{u} \tag{13}$$

where p is the pressure, ν is the viscosity of the gas, K is the permeability of the packed bed. Rearranging and writing in radial coordinates yields

$$\hat{u} = -\frac{K}{\mu}\frac{\partial p}{\partial r} \tag{14}$$

The fluid energy conservation equation is given by:

$$\varepsilon_b \frac{\partial e_f}{\partial t} + \nabla \cdot \left(\hat{u} e_f \right) = \nabla \cdot \left(\lambda_{eff,f} \nabla T_f \right) + k_h a_v (T_s - T_f) \tag{15}$$

where $e_f = \rho_f c_{p,f} T_f$ is the internal energy of the fluid, $\lambda_{eff,f}$ is the effective thermal conductivity, k_h is the interphase heat transfer coefficient and $a_v = 6(1 - \varepsilon_b)/d_p$ is the volume-specific surface area for spherical particles with a particle diameter d_p. In 1-D cylindrical coordinates,

$$\varepsilon_b \frac{\partial e_f}{\partial t} + \frac{1}{r} \frac{\partial}{\partial r} \left(r \hat{u} e_f \right) = \frac{1}{r} \frac{\partial}{\partial r} \left(r \lambda_{eff,f} \frac{\partial T_f}{\partial r} \right) + k_h a_v (T_s - T_f) \tag{16}$$

This system of equations is closed by the ideal gas equation:

$$p = \rho_f \bar{R} T_f \tag{17}$$

where $\bar{R}$ is the specific gas constant of the working fluid.

Solid Phase – The solid energy conservation equation is given by:

$$(1 - \varepsilon_b) \frac{\partial e_s}{\partial t} = \nabla \cdot \left(\lambda_{eff,s} \nabla T_s \right) + k_h a_v (T_f - T_s) + \Psi_s \Delta H_R \tag{18}$$

where $e_s = \rho_s c_{p,s} T_s$ is the internal energy of the solid, $\lambda_{eff,s}$ is the effective thermal conductivity and ΔH_R is the reaction enthalpy. In 1-D cylindrical coordinates:

$$(1 - \varepsilon_b) \frac{\partial e_s}{\partial t} = \frac{\partial}{\partial r} \left(r \lambda_{eff,s} \frac{\partial T_s}{\partial r} \right) + k_h a_v (T_f - T_s) + \Psi_s \Delta H_R \tag{19}$$

Shell – The energy balance across the outer shell is given by:

$$m_{shell} c_{p,shell} \frac{\partial T_{shell}}{\partial t} = \dot{q}_{int} - \dot{q}_{ext} \tag{20}$$

where

$$\dot{q}_{int} = A_3 h_{int} (T_f(r_3) - T_{shell}) \tag{21}$$

$$\dot{q}_{ext} = A_4 h_{ext} (T_{shell} - T_{HTF}) \tag{22}$$

3.4 Boundary Conditions

At the outer shell (boundary condition to eqs. 11, 13 and 15):

$$\hat{u}(r_3) = 0 \tag{23}$$

Imposed control pressure at the porous gas-feeding tube (boundary condition to eq. 9):

$$p(r_2) = p_c \tag{24}$$

Heat flux at the outer shell (boundary condition to eq. 15):

$$\lambda_{eff,f} \left. \frac{\partial T_f}{\partial r} \right|_{r=r_3} = -\dot{q}_{int} A_3 \tag{25}$$

No heat flux via the solid (boundary condition to eq. 18):

$$\left. \frac{\partial T_s}{\partial r} \right|_{r=r_2} = \left. \frac{\partial T_s}{\partial r} \right|_{r=r_3} = 0 \tag{26}$$

Flow temperature at the inner boundary if gas is streaming into the domain (boundary condition to eq. 15):

$$T_f(r_2) = T_{amb} \quad if \quad \hat{u}(r_2) > 0 \tag{27}$$

3.5 Material Properties

The correlations that have been used for the fluid and solid properties are listed in Table 1. The fluid internal energy is given by:

$$e_f = \gamma_0 + \gamma_1 T_f + \gamma_2 T_f^2 \tag{28}$$

where the numerical values of the coefficients in the case of CO_2 are $\gamma_0 = -1.845 \cdot 10^3 \frac{kJ}{kmol}$, $\gamma_1 = 2.572 \cdot 10^1 \frac{kJ}{kmol \cdot K}$ and $\gamma_2 = 1.051 \cdot 10^{-2} \frac{kJ}{kmol \cdot K^2}$, obtained by a fit to tabulated data (Moran and Shapiro, 2006).

The mass-specific heat capacity of a mixture of materials is calculated as a weighted average of each component according to

$$c_p = \left(X c_{p,A} + (1-X) c_{p,B} \right) \left(X M_A + (1-X) M_B \right)^{-1}, \ c_p \ \text{in} \ [\text{J} \cdot \text{kg}^{-1} \cdot \text{K}^{-1}] \tag{29}$$

The thermal conductivity of the bulk solid is a mass average of the two present materials:

$$\lambda_{s,bulk}(X, T) = X M_A \lambda_A(T) + (1-X) M_B \lambda_B(T) \tag{30}$$

and the corrected thermal conductivity given the particle void fraction (eq. 6) and in the absence of gas flow through the particle, according to (Loeb, 1954):

$$\lambda_s = (1 - \varepsilon_p) \lambda_{s,bulk} \tag{31}$$

The effective thermal conductivities for both phases are calculated according to the methodology presented in Kunii and Smith (1960) and Yagi and Kunii (1957). Contributions to the effective bed conductivity are made by (a) conduction through the fluid phase, (b) void-to-void radiation in the fluid phase, (c) conduction through the stagnant fluid film near the contact surface of two adjacent solid particles, (d) conduction through the solid phase and (e) solid-to-solid radiation. Heat transfer at the contact point of two adjacent solid particles is neglected.

The effective conductivity in the fluid phase incorporates effects (a) and (b):

$$\lambda_{eff,f} = \lambda_f \varepsilon_b \left(1 + \sigma \frac{h_{rv} \cdot d_p}{\lambda_f} \right) \tag{32}$$

where σ is the ratio between the distance of adjacent particle centers (in direction of heat flow) and the particle diameters. It has been set to unity. h_{rv} denotes the void-to-void radiative heat transfer coefficient:

$$h_{rv} = 0.9683 \cdot \left(1 + \frac{\varepsilon_b}{2(1-\varepsilon_b)} \cdot \frac{1-\epsilon_s}{\epsilon_s} \right)^{-1} \left(\frac{T_s}{100} \right)^3 \tag{33}$$

where ε_s is the emissivity of the solid particle. Note that the numerical value in this equation differs from the one presented in Yagi and Kunii (1957) due to unit conversion. The solid emissivity is assumed to be the emissivity of the material that occupies the outermost layer of a particle according to the shrinking core model (Yagi and Kunii, 1955):

$$\epsilon_s = \begin{cases} \epsilon_A \ \ if \ \ \frac{\partial X}{\partial t} > 0 \\ \epsilon_B \ \ if \ \ \frac{\partial X}{\partial t} < 0 \end{cases} \tag{34}$$

The effective conductivity in the fluid phase incorporates effects (c) – (e):

$$\lambda_{eff,s} = \lambda_f \frac{\beta(1-\varepsilon_b)}{\left(\frac{1}{\phi} + \frac{d_p h_{rs}}{\lambda_f} \right)^{-1} + \omega \left(\frac{\lambda_f}{\lambda_s} \right)} \tag{35}$$

where ϕ is the ratio between fluid film thickness and particle diameter and ω is the ratio between the effective length of a solid particle (in heat transfer direction) and the particle diameter, which is set to 2/3 (spherical particles). h_{rs} denotes the solid-to-solid radiative heat transfer coefficient:

$$h_{rs} = 0.9683 \cdot \left(\frac{\epsilon_s}{2-\epsilon_s}\right) \cdot \left(\frac{T_s}{100}\right)^3 \tag{36}$$

The interphase heat transfer coefficient k_h is determined by a Nusselt-correlation according to Gunn (1978):

$$Nu = (7 - 10\varepsilon_b + 5\varepsilon_b^2)(1 + 0.7Re^{0.2}Pr^{1/3}) + (1.33 - 2.4\varepsilon_b + 1.2\varepsilon_b^2)Re^{0.7}Pr^{1/3} \tag{37}$$

such that

$$k_h = Nu\frac{\lambda_f}{d_p} \tag{38}$$

Table 1: Correlations used for material properties of CO_2, CaO and $CaCO_3$.

	Units	Value/Correlation (T in K, P in Pa)	T(K)	Ref.
CO₂				
Dynamic Viscosity	kg·m⁻¹·s⁻¹	$1.038 \cdot 10^{-6} + 5.138 \cdot 10^{-8} \cdot T + 1.449 \cdot 10^{-13} \cdot P - 1.103 \cdot 10^{-11} \cdot T^2 - 1.11 \cdot 10^{-15} \cdot P \cdot T$	500-1300	Interpolated from (Fenghour et al., 1998)
Thermal Conductivity	W·m⁻¹·K⁻¹	$-9.76 \cdot 10^{-3} + 9.451 \cdot 10^{-5} \cdot T - 1.414 \cdot 10^{-8} \cdot T^2$ (at 1 bar)	700-1000	Interpolated from (Vesovic et al., 1990)
Specific Heat Capacity	J·kg⁻¹·K⁻¹	$453.6 + 1.6502 \cdot T - 1.2481 \cdot 10^{-3} \cdot T^2 + 3.782 \cdot 10^{-7} \cdot T^3$	300-1000	(Moran and Shapiro, 2006)
CaO				
Density	kg·m⁻³	3340	-	-
Thermal Conductivity	W·m⁻¹·K⁻¹	$8.831 \cdot 10^8 \cdot T^{-3.139} + 7.7511$	350 - 1300	Interpolated from (Kingery et al., 1954)
Specific Heat Capacity	J·mol⁻¹·K⁻¹	$49.954 + 4.8879 \cdot 10^{-3} \cdot T - 3.521 \cdot 10^{-7} \cdot T^2 + 4.62 \cdot 10^{-11} \cdot T^3 - 8.25 \cdot 10^5 \cdot T^{-2}$	298 – 3200	NIST Webbook
Emissivity	-	0.10	0-2000	(Kubarev, 2009)
CaCO₃				
Density	kg·m⁻³	2710	-	-
Thermal Conductivity	W·m⁻¹·K⁻¹	$135.8 \cdot T^{-0.752} + 1.064$	200 – 800	Interpolated from (Momenzadeh et al., 2018)
Specific Heat Capacity	J·mol⁻¹·K⁻¹	$-184.79 + 0.32322 \cdot T - 3688200 \cdot T^{-2} - 1.2974 \cdot 10^{-4} \cdot T^2 + 3883.5 \cdot T^{-1/2}$	298-1000	(Jacobs et al., 1981)
Emissivity	-	0.30	-	(Bramson, 1968)

3.6 Numerical Implementation

The governing conservation equations have been spatially discretized using finite volumes and temporally using a 4th order accurate Runge-Kutta scheme (Süli and Mayers, 2003). The reconstruction of boundary values and gradients use a 4th order accurate centered approximation. The model is implemented in C++ with post-processing done in MATLAB. The finite volume implementation uses a staggered approach for the location at which properties are known and calculated, i.e. densities, internal energy and pressure are stored at the cell centroids while velocities and gradients in general are calculated at the cell boundaries. This allows for a one-time calculation of the RHS terms in the conservation equations, which in turn assures that conservation of quantities is given. Temperature/pressure dependent material properties are evaluated using the prior step values to avoid computationally costly iterations.

4. Results

In the following, the simulation results of a representative scenario are presented. The geometrical parameters, boundary conditions, and material properties of this scenario are listed in Table 2. They correspond to a CaO/CaCO$_3$ system with 50% inert stabilization material (MgO) which has been selected for later experimental validation. The alternating charging/discharging states are held for 1 hour at a time, separated by a 10-minute linear ramp between the states, which reflects the thermal inertia of the system and helps to alleviate numerical constraints. In this baseline case, the total mass of solid reactant in the reactor is 0.8582 kg/m, yielding a theoretical chemical storage capacity of 1.571 MJ/m.

Table 2: Parameters for the representative scenario. Geometrical parameters and values of boundary conditions are on the left, material properties are on the right.

Parameter	Value	Parameter	Value
r_1	0.008 m	K	$7.64 \cdot 10^{-14}$ m^2
r_2	0.01 m	d_p	$2 \cdot 10^{-4}$ m
r_3	0.05 m	ε_b	0.4
r_4	0.051 m	c_0	133.322 Pa
T_{inlet}	298.15 K	c_1	10
$T_{ext,char.}$	1220 K	c_2	10.4022
$T_{ext,disc.}$	1150 K	c_3	-8792.3 K^{-1}
$P_{c,char.}$	$2 \cdot 10^4$ Pa	ρ_{bulk}^0	231 kg $\cdot$ m^{-3}
$P_{c,disc.}$	$5 \cdot 10^5$ Pa		

All presented integrated quantities are given per unit length of reactor tube. The time-integrated energy flux across the walls of the outer shell is defined as:

$$Q_{ht}(t) = A_3 \int_0^t \dot{q}_{int}(t')dt' \tag{39}$$

The time-integrated energy flux across the inner tube is defined as:

$$Q_{inlet}(t) = A_2 \int_0^t u(r_2,t')e_f(r_2,t')dt' \tag{40}$$

Figure 2 (a) and (b) show the boundary conditions (HTF temperature T_{HTF} and control pressure p_c) as a function of time. Figure 2 (c) shows the mean reaction extent of the total volume as a function of time, calculated as:

$$\chi_{Reactor} = \frac{\int_{r_2}^{r_3} r' \mathrm{X}(r')dr'}{\int_{r_2}^{r_3} r'dr'} \tag{41}$$

In this particular configuration, the control pressure p_c applied during discharging is relatively high, therefore discharging proceeds faster than charging. In a real system, p_c would be controlled to allow the reactor to discharge at a specified rate. Figure 2 (d) shows the change of energy in the reactor over time broken down to the contributions of the reaction enthalpy, fluid enthalpy, and solid sensible heat. While the enthalpy of the fluid is quite insignificant, the sensible heat stored in the solid phase has an impact on the total reactor energy. In this specific scenario, the total reactor heat capacity is lowered as the reaction proceeds in the direction of calcium oxide, thereby gradually lowering the heat stored in the solid phase despite near-constant temperatures. Figure 2 (e) shows the energy flows into and out of the reactor. Note the convention of positive energy flows in positive r-direction. An important observation is the

gradual energy loss through the gas that leaves/enters the reactor through the inner tube. During the discharging step, the gas leaves at a very high temperature. It is then stored outside the reactor where, in a worst-case scenario, it cools down to ambient temperature before being pumped back into the reactor during the next charging phase. In practice, these losses could be mitigated by either insulating the external gas storage or passing the outflow vertically through the SHS (Fig. 1) in a separated tube.
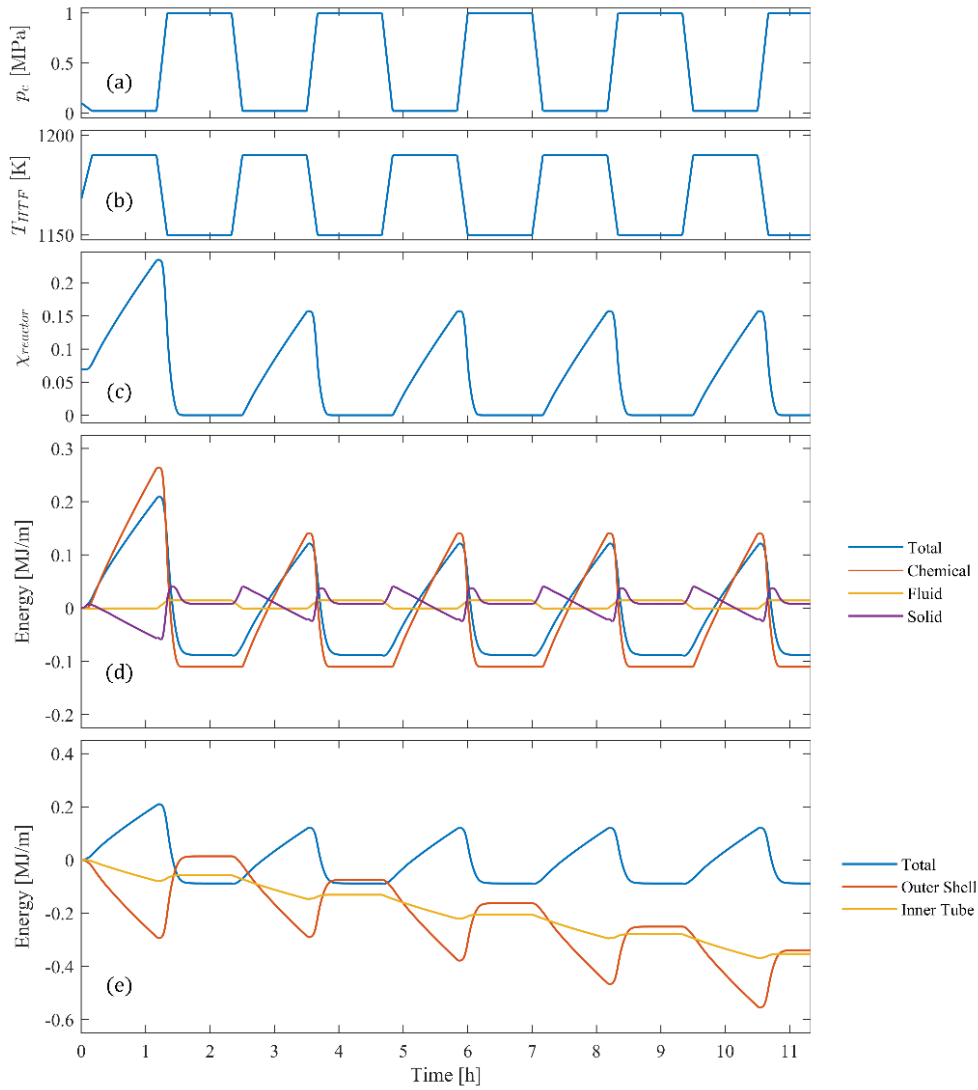

Figure 2: (*a*) Control pressure p_c at the inner boundary as a function of time, (*b*) HTF temperature T_{HTF} as a function of time, (*c*) Reactor charge state $\chi_{reactor}$ as a function of time, (*d*) Variation of energy stored in the reactor and fractions stored in the chemical reaction, sensible energy of the solid phase and enthalpy of the fluid phase as a function of time, (*e*) Variation of energy stored in the reactor and time-integrated heat fluxes over the outer shell and the inner tube as a function of time.

5. Conclusions

A detailed two-phase heat and mass transfer model of an annular bed reactor for thermochemical energy storage has been presented. The material properties, which depend on both the temperature and the reactant composition, are presented. The results of a numerical simulation of a representative reactor system are presented and the most significant effects are discussed.

As a next step, this model will be experimentally validated using a lab-scale reactor setup using the thermal decomposition of calcium oxide into calcium carbonate and CO_2. Following this, a number of parametrical studies can be performed to study the effects of geometry, chemistry and material morphology on this system. This will help to identify reactor configurations and material properties that are suitable for a given application.

6. Acknowledgements

7. References

Agrafiotis, C., Becker, A., Roeb, M., Sattler, C., 2016. Exploitation of thermochemical cycles based on solid oxide redox systems for thermochemical storage of solar heat. Part 5: Testing of porous ceramic honeycomb and foam cascades based on cobalt and manganese oxides for hybrid sensible/thermochemical heat s. https://doi.org/10.1016/j.solener.2016.09.013

Agrafiotis, C., Roeb, M., Sattler, C., 2015. Hybrid sensible/thermochemical solar energy storage concepts based on porous ceramic structures and redox pair oxides chemistry. Energy Procedia 69, 706–715. https://doi.org/10.1016/j.egypro.2015.03.081

André, L., Abanades, S., Flamant, G., 2016. Screening of thermochemical systems based on solid-gas reversible reactions for high temperature solar thermal energy storage. https://doi.org/10.1016/j.rser.2016.06.043

Block, T., Schmü, M., 2016. Metal oxides for thermochemical energy storage: A comparison of several metal oxide systems. https://doi.org/10.1016/j.solener.2015.12.032

Bramson, M.A., 1968. Emissivity of Various Materials. In: Infrared Radiation. Optical Physics and Engineering. Springer, Boston, MA. https://doi.org/10.1119/1.1973963

Bush, H.E., Loutzenhiser, P.G., 2018. Solar electricity via an Air Brayton cycle with an integrated two-step thermochemical cycle for heat storage based on Fe2O3/Fe3O4 redox reactions: Thermodynamic and kinetic analyses. Sol. Energy 174, 617–627. https://doi.org/10.1016/j.solener.2018.09.043

Davis, M.E., Watson, L.T., 1986. Mathematical Modeling of Annular Reactors. Chem. Eng. J. 33, 133–142.

Davis, M.E., Yamanis, J., 1984. Axial Dispersion in the Annular Bed Reactor. Chem. Eng. Commun. 25, 1–10. https://doi.org/10.1080/00986448408940094

Dixon, A.G., Nijemeisland, M., 2001. CFD as a Design Tool for Fixed-Bed Reactors. https://doi.org/10.1021/ie001035a

Fenghour, A., Wakeham, W.., Vesovic, V., 1998. The Viscosity of Carbon Dioxide. J. Phys. Chem. Ref. Data 27, 31–44.

Gigantino, M., Kiwic, D., Steinfeld, A., 2019. Thermochemical energy storage via isothermal carbonation-calcination cycles of MgO-stabilized SrO in the range of 1000–1100 °C. Sol. Energy 188, 720–729. https://doi.org/10.1016/j.solener.2019.06.046

Gunn, D.J., 1978. Transfer of Heat or Mass to Particles in Fixed and Fluidised Beds. Int. J. Heat Mass Transf. 21,

467–476.

Jacobs, G.K., Kerrick, D.M., Krupka, K.M., 1981. The high-temperature heat capacity of natural calcite (CaCO3). Phys. Chem. Miner. 7, 55–59. https://doi.org/10.1007/BF00309451

Kingery, W.D., Francl, J., Coble, R.L., Vasilos, T., 1954. Thermal Conductivity: X, Data for Several Pure Oxide Materials Corrected to Zero Porosity. J. Am. Ceram. Soc. 37, 107–110. https://doi.org/10.1111/j.1551-2916.1954.tb20109.x

Kubarev, V.V., 2009. Features of the Drummond Light of Calcium Oxide. Opt. Spectrosc. 106, 242–247. https://doi.org/10.1134/S0030400X09020155

Kunii, D., Smith, J.M., 1960. Heat transfer characteristics of porous rocks. AIChE J. 6, 71–78. https://doi.org/10.1002/aic.690060115

Kuravi, S., Trahan, J., Goswami, D.Y., Rahman, M.M., Stefanakos, E.K., 2013. Thermal energy storage technologies and systems for concentrating solar power plants. Prog. Energy Combust. Sci. 39, 285–319. https://doi.org/10.1016/j.pecs.2013.02.001

Kyaw, K., Matsuda, H., Hasatani, M., 1996. Applicability of Carbonation/Decarbonation Reactions to High-Temperature Thermal Energy Storage and Temperature Upgrading. J. Chem. Eng. Japan 29, 119–125.

Loeb, A.L., 1954. Thermal Conductivity: VIII, A Theory of Thermal Conductivity of Porous Materials. J. Am. Ceram. Soc. 37, 96–99. https://doi.org/10.1111/j.1551-2916.1954.tb20107.x

Momenzadeh, L., Moghtaderi, B., Buzzi, O., Liu, X., Sloan, S.W., Murch, G.E., 2018. The thermal conductivity decomposition of calcite calculated by molecular dynamics simulation. Comput. Mater. Sci. 141, 170–179. https://doi.org/10.1016/j.commatsci.2017.09.033

Moran, M.J., Shapiro, H.N., 2006. Fundamentals of Engineering Thermodynamics, John Wiley & Sons, Inc. https://doi.org/10.1038/1811028b0

Muroyama, A.P., Schrader, A.J., Loutzenhiser, P.G., 2015. Solar electricity via an Air Brayton cycle with an integrated two-step thermochemical cycle for heat storage based on Co3O4/CoO redox reactions II: Kinetic analyses. Sol. Energy 122, 409–418. https://doi.org/10.1016/j.solener.2015.08.038

Romero, M., Steinfeld, A., 2012. Concentrating solar thermal power and thermochemical fuels. Energy Environ. Sci. 5, 9234–9245. https://doi.org/10.1039/c2ee21275g

Ströhle, S., Haselbacher, A., Jovanovic, Z.R., Steinfeld, A., 2017. Upgrading sensible-heat storage with a thermochemical storage section operated at variable pressure: An effective way toward active control of the heat-transfer fluid outflow temperature. Appl. Energy 196, 51–61. https://doi.org/10.1016/j.apenergy.2017.03.125

Ströhle, S., Haselbacher, A., Jovanovic, Z.R., Steinfeld, A., 2014. Transient discrete-granule packed-bed reactor model for thermochemical energy storage. Chem. Eng. Sci. 117, 465–478. https://doi.org/10.1016/j.ces.2014.07.009

Süli, E., Mayers, D.F., 2003. An Introduction to Numerical Analysis.

Vesovic, V., Wakeham, W.A., Olchowy, G.A., Sengers, J. V., Watson, J.T.R., Millat, J., 1990. The Transport Properties of Carbon Dioxide. J. Phys. Chem. Ref. Data 19, 763–808. https://doi.org/10.1063/1.555875

Yagi, S., Kunii, D., 1957. Studies on effective thermal conductivities in packed beds. AIChE J. 3, 373–381. https://doi.org/10.1002/aic.690030317

Yagi, S., Kunii, D., 1955. Studies on combustion of carbon particles in flames and fluidized beds. Symp. Combust. 5, 231–244. https://doi.org/10.1016/S0082-0784(55)80033-1

Zanganeh, G., Commerford, M., Haselbacher, A., Pedretti, A., Steinfeld, A., 2014. Stabilization of the outflow temperature of a packed-bed thermal energy storage by combining rocks with phase change materials. Appl. Therm. Eng. 70, 316–320. https://doi.org/10.1016/j.applthermaleng.2014.05.020

Zanganeh, G., Khanna, R., Walser, C., Pedretti, A., Haselbacher, A., Steinfeld, A., 2015. Experimental and numerical investigation of combined sensible-latent heat for thermal energy storage at 575°C and above. Sol. Energy 114, 77–90. https://doi.org/10.1016/j.solener.2015.01.022